

1 **Unravelling Landslide Failure Mechanisms with Seismic Signal**
2 **Analysis for Enhanced Pre-Survey Understanding**

3 Jui-Ming Chang^{1,2}, Che-Ming Yang^{3*}, Wei-An Chao^{1,2}, Chin-Shang Ku⁴, Ming-Wan Huang^{3,5}, Tung-
4 Chou Hsieh², Chi-Yao Hung⁶

5
6 ¹Department of Civil Engineering, National Yang Ming Chiao Tung University, Hsinchu 30010, Taiwan

7 ²Disaster Prevention and Water Environment Research Center, National Yang Ming Chiao Tung
8 University, Hsinchu 30010, Taiwan

9 ³Department of Civil and Disaster Prevention Engineering, National United University, Miaoli 36063,
10 Taiwan

11 ⁴Institute of Earth Sciences, Academia Sinica, Taipei 11529, Taiwan

12 ⁵He Yu Engineering Consultants Co. Ltd., Taichung 40642, Taiwan

13 ⁶Department of Soil and Water Conservation, National Chung Hsing University, Taichung 40227, Taiwan

14 *Correspondence to:* Che-Ming Yang (stanleyyangcm@nuu.edu.tw)

16 **Abstract**

17 Seismic signals, with their remote and continuous monitoring advantages, have been instrumental in
18 unveiling various landslide characteristics and have been widely applied in the past decades. However, a
19 few studies have extended these results to provide geologists with pre-survey information, thus enhancing
20 the understanding of the landslide process. In this research, we utilize the deep-seated Cilan Landslide
21 (CL) as a case study and employ a series of seismic analyses, including spectrogram analysis, single force
22 inversion, and geohazard location. These techniques enable us to determine the physical processes, sliding
23 direction, mass amount estimation, and location of the deep-seated landslide. Through efficient discrete
24 Fourier transform for spectrograms, we identified three distinct events, with the first being the most
25 substantial. Further analysis of spectrograms using a semi-log frequency axis generated by discrete
26 Stockwell transform revealed that Event 1 consisted of four sliding failures occurring within thirty
27 seconds with decreasing sliding mass. Subsequent Events 2 and 3 were minor toppling and rockfalls,
28 respectively. Geohazard location further constrained the source location, indicating that Events 1 and 2
29 likely originated from the same slope. Subsequently, the sliding direction retrieved from single force
30 inversion and volume estimation was determined to be 153.67° and $557,118 \text{ m}^3$, respectively, for the CL.
31 Geological survey data with drone analysis corroborated the above seismological findings, with the
32 sliding direction and source volume estimated to be around 148° and $664,926 \text{ m}^3$, respectively, closely
33 aligning with the seismic results. Furthermore, the detailed dynamic process observed in the spectrogram
34 of Event 1 suggested a possible failure mechanism of CL involving advancing, retrogressing, enlarging,
35 or widening. Combining the above mechanism with geomorphological features identified during field
36 surveys, such as the imbrication-like feature in the deposits and the gravitational slope deformation, with
37 event video, infers the failure mechanism of retrogression of the Event 1 after shear-off from the toe.
38 Then, the widening activity was caused by the failure process for subsequent events, as Events 2 and 3.
39 This case study underscores the significance of remote and adjacent seismic stations in offering
40 seismological-based landslide characteristics and a time vision of the physical processes of landslides,
41 thereby assisting geologists in landslide observation and deciphering landslide evolution.

42 **Keywords:** Cilan Landslide, Spectrograms, Discrete Stockwell Transform, Landslide Failure Mechanism

43 **1 Introduction**

44 In recent decades, seismology has expanded in scope to include mass movements on the Earth's
45 surface since the first observation of landslide signals during volcanic eruptions (Kanamori and Given,
46 1982). After that, the application of associated analyses from seismology, particularly in landslide
47 research has gradually increased (Brodsky et al., 2003; Vilajosana et al., 2008; Feng, 2011; Allstadt et al.,
48 2013; Hibert et al., 2014; Dietze et al., 2017).

49 Different seismic signal frequencies play distinct roles in landslide characterization. Low-
50 frequency seismic signals, typically below 0.1 Hz, have been employed to approximate the source location,
51 estimate the sliding direction, and reconstruct its trajectory (Yamada et al., 2013; Hibert et al., 2015; Chao
52 et al., 2018). These signals are generated by ground rebound from slope failure, which were detected in
53 the cases of massive landslides with areas greater than 10,000 m² or volumes exceeding 100,000 m³ (Kuo
54 et al., 2018). Moreover, low-frequency signals have unique characteristics that can be used as
55 distinguishing features. The signal source is assumed to be a point source that undergoes loading and
56 unloading processes. By comparing synthetic and observed waveforms from a single force mechanism
57 using a grid search and by adapting data from seismic stations, the approximate source location and
58 inverted force direction of a landslide can be determined (Chao et al., 2017). The magnitude of the
59 inverted force is related to the landslide scale (Ekström and Stark, 2013; Chao et al., 2016). However,
60 because of the longer wavelengths associated with low-frequency signals, the accuracy of the source
61 constraints is reduced compared to higher-frequency signals.

62 High-frequency seismic signals (>1Hz) have different functions in landslide research. They are,
63 for example, used to recognize the details of the source mechanism (Provost et al., 2018; Weng et al.,
64 2022) and the constraints of the source location (Chen et al., 2013; Walsh et al., 2017; Yang et al., 2022).
65 Seismic time-frequency spectrograms have been identified as the source type. Compared with the right
66 triangle spectrogram feature associated with the onset of the P-wave of earthquakes, landslides typically
67 exhibit a cigar-shaped feature with a linear (Suriñach et al., 2005; Moretti et al., 2012) or semi-log
68 (Dammeier et al., 2011) frequency axis resulting from the Fourier transform. More recently, other
69 spectrogram features, such as V-shaped, column-shaped, and pulse-like features corresponding to the

70 failure mechanisms of sliding, toppling, and rockfall, respectively (Chang et al., 2021) have been observed
71 in spectrograms generated by the Stockwell transform with a semi-log plot. However, the advantages and
72 disadvantages of these two linear and semi-log label transforms have not been thoroughly addressed.
73 Through spectrogram recognition, the duration of the physical processes of a landslide can be determined.

74 There are three methods used for the source location: (1) time difference (Chen et al., 2013; Fuchs
75 et al., 2018; Manconi and Mondini, 2022), (2) amplitude decay (Aki and Ferrazzini, 2000; Walter et al.,
76 2017), and (3) the azimuth of polarization analysis (Guinau et al., 2019). The time-difference method
77 calculates the time difference between pairs of stations using a velocity model to constrain possible source
78 locations. The accuracy of location determination depends upon the station coverage of the source area
79 (Chang et al., 2023). The amplitude source location method considers the decay of the seismic amplitude
80 with distance. However, the results can be influenced by the distribution of the source-station distances,
81 which often leads to the source location being biased toward the station with the highest amplitude caused
82 by site effect (Chang et al., 2023). Although the first and second methods are commonly used in landslide
83 research, the azimuth of polarization analysis has rarely been discussed in landslide source analysis.
84 Guinau et al. (2019) adapted the polarization to retrieve the source azimuth and locate the rockfall by
85 recognizing P- and S-waves through particle motion.

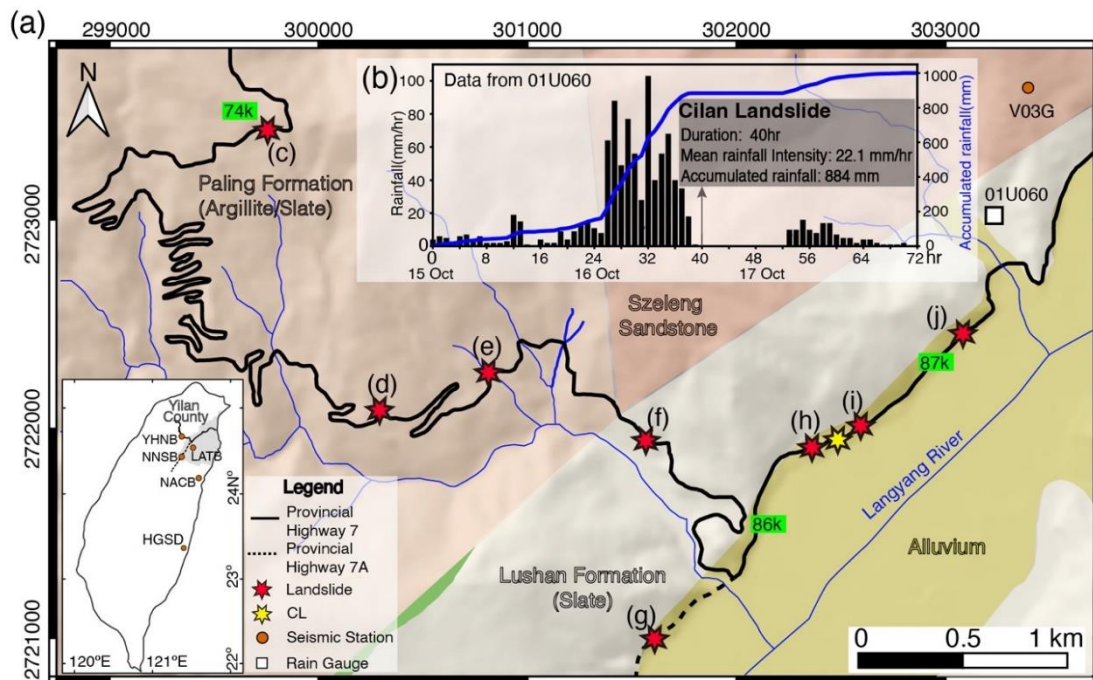
86 Investigations into low- and high-frequency seismic signals provide invaluable perspectives on
87 landslides. However, few studies have sorted out the information as preliminary knowledge to geologists,
88 especially for the continuous time vision of the failure process. Historically, geologists relied solely on
89 field and drone surveys conducted before and after landslide events to depict landslide failure mechanisms,
90 thereby lacking associated information on temporal evolution to link different phases of landslide activity.
91 Geologists need to speculate on the connection of landslide activity to the geological model. However,
92 seismological-based information complements this approach by providing temporal context. Therefore,
93 this study integrates seismic results with landslide investigation (field and drone surveys) to illustrate
94 constructing a landslide evolution model.

95

96 2 Background information

97 2.1 Landslides During Typhoon Nesat

98 Torrential rainfall resulting from the interaction between Typhoon Nesat and the winter monsoon
99 lashed Yilan County in northeast Taiwan from 15 October to 17 October 2022 (Fig. 1a; the time in this
100 research all shows in local time UTC+8). The accumulated precipitation reached 1,000 mm in three days,
101 with a peak rainfall intensity of 103 mm hr⁻¹. (Fig. 1b). This accumulation exceeded the landslide
102 threshold of 550 mm, as documented by the Agency of Rural Development and Soil and Water
103 Conservation (<https://246.ardswc.gov.tw/>; last accessed on 30 October 2024). Consequently, many
104 rainfall-induced landslides occurred. **Most landslides accumulated next to roads (Fig. S1)**, destroying
105 sections of two vital provincial highways: No. 7 (Northern Cross-Island Highway) and No. 7A (Fig. 1a).
106 The Directorate General of Highways, Taiwan, reported nine sections damaged by landslides (Figs. 1c-
107 1j; Table S1). Among these, three roadbed washouts characterized by argillite/slate were observed in the
108 Paling Formation (Figs. 1c-1e), whereas a landslide composed of slate covered a road section in the
109 Lushan Formation (Fig. 1f). Additionally, four debris flow events occurred near the boundary between
110 the Lushan Formation and the alluvium (Figs. 1g-1j). As of 22 October 2022, these events left 302 people
111 stranded, resulting in one missing person. In addition to these nine events, a deep-seated landslide, known
112 as the Cilan landslide (CL), occurred in the Lushan Formation. Initially, an individual captured a part of
113 the CL process on video, revealing two distinct stages of material sliding (Fig. S2). According to the video
114 footage, the initial landslide was formed by exposure to the bare earth. The video captured the subsequent
115 failures. The first body in the footage slid between 0-20 seconds, and the following failure occurred at the
116 20-second mark in the video recording. Then, the Directorate General of Highways in Taiwan identified
117 the precise location of the landslide (Fig. S3 and yellow star in Fig. 1a) and provided an approximate
118 occurrence time of 4:00 PM on 16 October 2022.

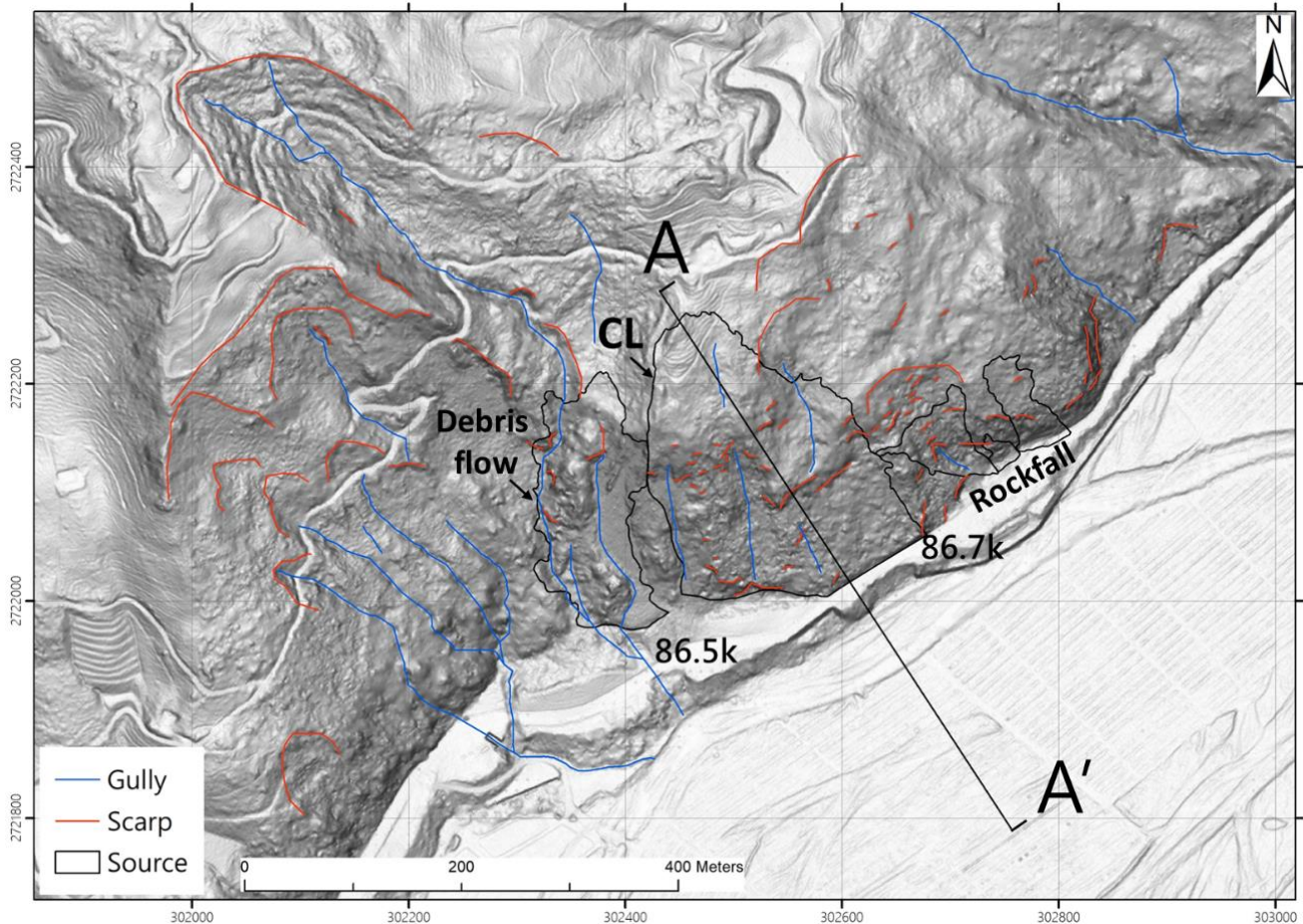


119

120 Figure 1 (a) Regional geologic map of roadside landslides, seismic station, and rain gauge (Fei and Chen,
121 2013). The grey-shaded area in the map of Taiwan (lower left) represents Yilan County. (b) Rainfall data
122 of rain gauge 01U060 during the typhoon. The rain episode started on 15 October 2022 at 00:00 AM
123 (Local time UTC+8). (c)-(j) In situ photos for landslides. All photos are open data from the Directorate
124 General of Highways, Taiwan (Table S1). The k in the map/photos indicates the milestone (in kilometers)
125 of two provincial highways.

126 **2.2 Topographic Feature Near the CL**

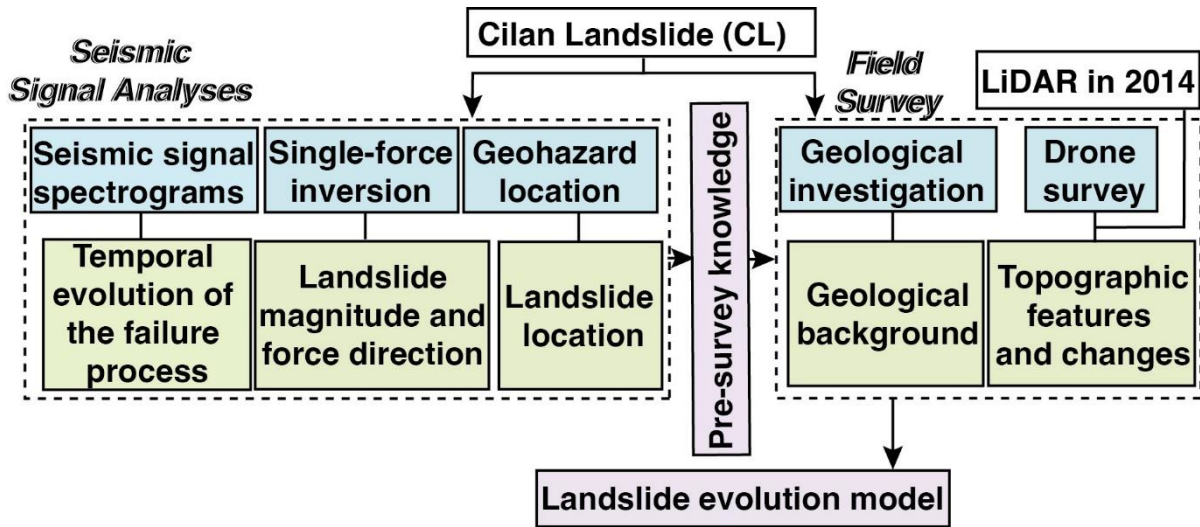
127 According to 1-m high-resolution LiDAR-derived slope inclination map (Fig. 2), several
128 prominent features were evident near the CL. On the west side of the CL, a concave slope displayed
129 distinct scarps and gullies. These features strongly indicated that the concave slope was subject to erosion.
130 Conversely, the eastern roadside slopes of the CL revealed a contrasting topography characterized by
131 numerous scarplets with several gullies and convex slopes, all prone to rockfalls. Within this context,
132 slopes at the 86.5 km and 86.7 km milestones along Provincial Highway No. 7 experienced a debris flow
133 on the gentler portions (Fig. 1h) and talus deposits on the steeper sections (Fig. 1i).



134 Figure 2 Topographic feature interpretation with 1 m high-resolution LiDAR slope map in 2014 before
135 the CL. The AA' is for the topographic profile in Fig. 7b. The black line polygons indicate the
136 source boundary of slope failures.
137

138 **3. Methods**

139 The study aims to leverage seismic analysis as preliminary knowledge to aid in illustrating the
140 landslide evolution model of the CL. To achieve this, we conducted a series of seismic signal analyses,
141 including seismic signal spectrograms, single force inversion (SF), and geohazard location (GeoLoc).
142 These analyses provide insights into the temporal evolution of the failure process, landslide magnitude,
143 inverted force direction, and landslide location constraints. Geologists use these results to gain a basic
144 understanding of the CL prior to conducting a field survey. The field survey consists of two parts:
145 geological investigation and drone survey. The former provides geological background information,
146 while the latter, joining LiDAR in 2014, captures topographic features and changes post-CL. The
147 combined results from the seismic signal analyses and field surveys support the development of the most
148 plausible landslide evolution model. The flowchart is depicted in Fig. 3.



149 Figure 3 Flowchart of this study. The blue, green, and purple backgrounds are relevant to the methodology,
150 results, and discussion.
151

152

153 3.1 Seismic signal spectrograms

154 The study investigated time-frequency spectrograms based on the power spectral density (PSD)
155 of the discrete Fourier transform (DFT), as well as the power spectrum (PS) of the discrete Stockwell
156 transform (DST). The DST of Eq. (1) was derived from Eq. (2), while f , τ , t , and α were derived from Eqs.
157 (3)-(7).

$$158 \text{ DST: } s[p\Delta t, \frac{l}{N\Delta t}] = \sum_{m=1}^{N-1} H[\frac{l+m}{N\Delta t}] e^{-2\pi^2 \frac{m^2}{l^2}} e^{2\pi i \frac{mp}{N}} \quad (1)$$

$$159 \text{ DFT: } H[\frac{l}{N\Delta t}] = \frac{1}{N} \sum_{k=0}^{N-1} h[k\Delta t] e^{-2\pi i \frac{lk}{N}} \quad (2)$$

$$160 f = \frac{l}{N\Delta t} \quad , l = 0, 1, 2 \dots N - 1 \quad (3)$$

$$161 \tau = p\Delta t \quad , p = 0, 1, 2 \dots N - 1 \quad (4)$$

$$162 \alpha = \frac{m}{N\Delta t} \quad , m = 0, 1, 2 \dots N - 1 \quad (5)$$

$$163 t = k\Delta t \quad , k = 0, 1, 2 \dots N - 1 \quad (6)$$

$$164 PS = s[p\Delta t, \frac{l}{N\Delta t}]^2 \quad (7)$$

165 where Δt is the time sample interval, τ denotes the time of spectral localization, N is the total number of
166 data points, α , and f control the discrete frequency point, and $h[t]$ is the discrete-time series seismic data.

167 In the context of landslides, the predominant frequencies of ground vibrations typically range from
168 1 Hz to 10 Hz (Chang et al., 2021). To represent the power distribution within this range precisely, we
169 configured the DFT analysis to have time and frequency resolutions of 1.28 seconds and 0.39 Hz,
170 respectively. This configuration effectively captured the pertinent frequency information while retaining
171 an acceptable time resolution. Also, a cumulative PSD plot was obtained by summing the PSD values at
172 discrete time intervals. Alternately, applying DST instead of DFT allows for either enhanced frequency
173 resolution for the lower frequencies through broader time windows or improved time resolution for the
174 higher frequencies through narrower windows. In this study, we opted for a time window of 0.05 seconds
175 and a frequency resolution of 0.30 Hz in the DST analysis. These parameters provided superior frequency
176 and time resolutions, enabling the capture of intricate spectrogram details.

177 The scale of the frequency axis on the spectrograms profoundly influences recognition and
178 interpretation within the target frequency range of 1 Hz to 10 Hz. Therefore, we incorporated linear and
179 logarithmic frequency axes into the spectrograms. By judiciously selecting window lengths, time and
180 frequency resolutions, and frequency axes, we facilitated effective visualization and analysis of the power
181 distribution in seismic signals, particularly within the frequency range pertinent to landslide occurrences.

182 **3.2 Single-force inversion (SF)**

183 Single-force inversion (SF) is a technique used in the near-real-time landquake monitoring system
184 (NRLAMS) to extract the possible force direction and magnitude of a landslide (Chao et al., 2017; Chang
185 et al., 2024). Before conducting the SF analysis, we performed several preprocessing steps on the seismic
186 signals. First, we applied a bandpass filter between 0.02 Hz and 0.05 Hz to isolate the frequency range
187 for large-scale landslides (volume $> 10^5 \text{ m}^3$ or area $> 10^4 \text{ m}^2$, as defined by Chen, 2015). This frequency
188 range is associated with landslide-related signals in Taiwan (Chao et al., 2017). In addition, we
189 transformed the original horizontal components of the seismic data into radial and tangential components.
190 Different weightings in the SF correspond to the signal-to-noise ratio (SNR) (Table S2), the ratio between
191 the absolute peak amplitude and the average absolute amplitude from the entire signal trace.

192 Subsequently, the SF analysis simulated synthetic waveforms assuming a source depth of 1 km,
193 and Green's functions were calculated based on the surface wave velocity model proposed by Shin and
194 Chen (1998). Different synthetic waveforms were generated using different settings of force direction,
195 magnitudes, and dips. These waveforms were compared with the observed signals regarding fitness values,
196 the sum of the maximum normalized cross-correlation coefficient, and variance reduction. The highest
197 fitness values corresponding to the inverted force parameters were determined. Furthermore, a parameter
198 of inverted force magnitude (unit: Newton) of SF could be used to estimate the landslide mass through
199 the empirical formula, $\text{mass (kg)} = 0.405 \times \text{force magnitude}$ (Chao et al., 2016). Assuming a rock density
200 of approximately $2,600 \text{ kg m}^{-3}$, the estimated landslide mass could be roughly converted to landslide
201 volume. The seismic data for the SF analysis were obtained from a broadband array in Taiwan for seismic
202 networks (Kao et al., 1998). A more detailed methodology associated with the parameter setting and
203 procedure is provided by Chao et al. (2017).

204 **3.3 Geohazard location**

205 The geohazard location (GeoLoc) method, as outlined by Chang et al. (2021), synergizes the cross-
206 correlation (CC) method (Chen et al., 2013) with the amplitude source location (ASL) method (Aki and
207 Ferrazzin, 2000) to pinpoint potential landslide locations using seismic signals in the frequency range of
208 over 1 Hz. This approach initially filtered the seismic data between 1 Hz and 3 Hz. Subsequently, the
209 SNR was calculated as a ratio between the short-term average (± 5 s from the maximum envelope
210 amplitude) and the long-term average of a 180-second target trace. A threshold of SNR larger than 1.7
211 was applied to select the available waveforms for further analysis. The selected frequency range and SNR
212 threshold were empirically established based on extensive-scale landslides in Taiwan (Chen et al., 2013).

213 The CC method calculates the maximum cross-correlation coefficient between each station pair
214 to extract the travel time difference. This difference was then used with a three-dimensional velocity
215 model (Wu et al., 2007) and grid search to define the misfit function. Simultaneously, the ASL method
216 gauges its misfit function by optimizing the fit of the amplitude decay curve. By individually sorting the
217 misfit functions across all search grids, both methodologies yielded reliable source locations for landslides.
218 The potential source locations were identified when the grids had relative fitness values greater than 0.95
219 Chang et al. (2023). The detailed algorithm of GeoLoc can be found in Chang et al. (2021).

220 Seismic data for GeoLoc analysis were collected from various sources (Table S3), including
221 temporary stations maintained by the Comprehensive Landquake Monitoring Lab (CoLLab), National
222 Yang Ming Chiao Tung University, a broadband array in Taiwan for seismology, and the Central Weather
223 Administration, Taiwan.

224 **3.4 Field survey**

225 The field survey encompassed two integral components: drone survey and geological
226 investigation on 19 October 2022. For the drone survey, we conducted a series of vertical and inclined
227 aerial photos along the CL using the DJI Phantom 4. These photos were input for the photogrammetry
228 software Pix4D, which generated a digital surface model (DSM). Through the DSM, the
229 geomorphological features after the CL could be depicted. Additionally, by combining the LiDAR data

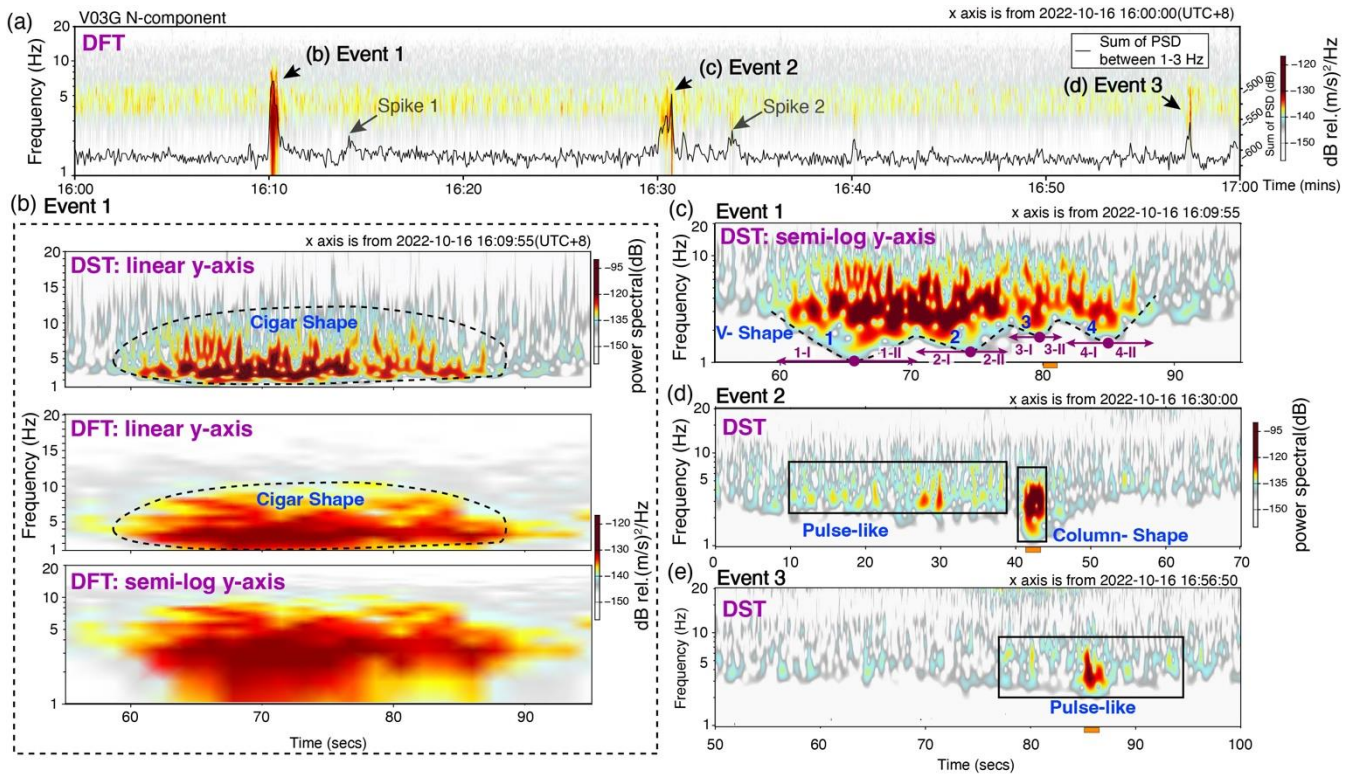
230 from 2014 with **digital elevation model (DEM)**, we could observe the differences in topography before
231 and after the CL event. **The LiDAR DEM was obtained from the Ministry of the Interior, Taiwan. The**
232 **drone-derived DSM was produced using ground control points via the e-GNSS service (Virtual Reference**
233 **Station Real-Time Kinematic technology) provided by the Ministry of the Interior, Taiwan. The vertical**
234 **root mean square errors for the LiDAR DEM and the drone-derived DSM were found to be 0.5 m and 0.2**
235 **m, respectively.** On the other hand, the geological investigation focused on road inspection and outcrop
236 observation before and after the CL, respectively. The road inspection documented the status of slope
237 protection, particularly regarding crack geometry. The outcrop observation recorded the strike and dip for
238 cleavage, joints, and bedding near the CL.

239 **4. Result**

240 **4.1 Seismic spectrograms for the CL**

241 According to the one-hour spectrogram generated through DFT analysis of V03G (Fig. 4a), the
242 resulting spectrograms revealed three distinct high-power onsets potentially corresponding to different
243 landslide events. The first event, labeled Event 1, occurred from 16:10:00 to 16:10:30. The cigar-shaped
244 features of the spectrograms indicated a landslide process when the spectrograms were analyzed using a
245 linear frequency axis (Fig. 4b). However, when the DST was modified to a semi-log graph, the lower
246 bounds of the high PSD displayed V-shaped spectrogram features (Fig. 4c). Such V-shaped patterns were
247 not discernible in the spectrograms obtained using the DFT because of the inherent limitations imposed
248 by the frequency and time resolution (Fig. 4b). The V-shape is associated with sliding behavior (Chang
249 et al., 2021), which involves phases of acceleration and deceleration of the landslide materials separated
250 by the lowest point of the V-shape. In Event 1, the four V-shaped events were interconnected, and their
251 lowest points (depicted as purple dots in Fig. 4c) gradually shifted to higher frequencies, indicating a
252 reduction in the sliding material volume. **The clear and consistent pattern indicates that the signals are**
253 **most likely from a single landslide event.** As a result, the event was the initial sliding of massive mass,
254 which also generated signals within the frequency range of 0.02 Hz to 0.05 Hz, detectable by the SF
255 method (See following subsection). With smaller volumes involved in the subsequent sliding events, the
256 corresponding signals in the low-frequency range could not be generated.

257 Approximately 20 min after Event 1, Event 2 occurred, and the spectrogram revealed a sequence
 258 of continuous pulse-like features (black rectangle in Fig. 4d). However, the frequency bands associated
 259 with these pulse-like features overlapped with ambient noise. Certain pulse-like features could be
 260 discerned, indicating continuous rock-ground impacts in the form of rockfalls. Subsequently, a column-
 261 like shape emerged in the spectrogram, an interaction between the substantial mass and the slope or
 262 ground (dashed black rectangle in Fig. 4d). This phenomenon referred to processes such as toppling or
 263 rockfalls on overhanging slopes or similar mechanisms. Approximately 26 min later, Event 3 emerged,
 264 presenting spectrogram features analogous to the continuous rock-ground impacts observed in Event 2
 265 (black rectangle in Fig. 4e). In particular, a gradual decrease in the PSD and PS values and signal durations
 266 was evident from Events 1 to 3, presenting a reduction in the scale of the landslide.



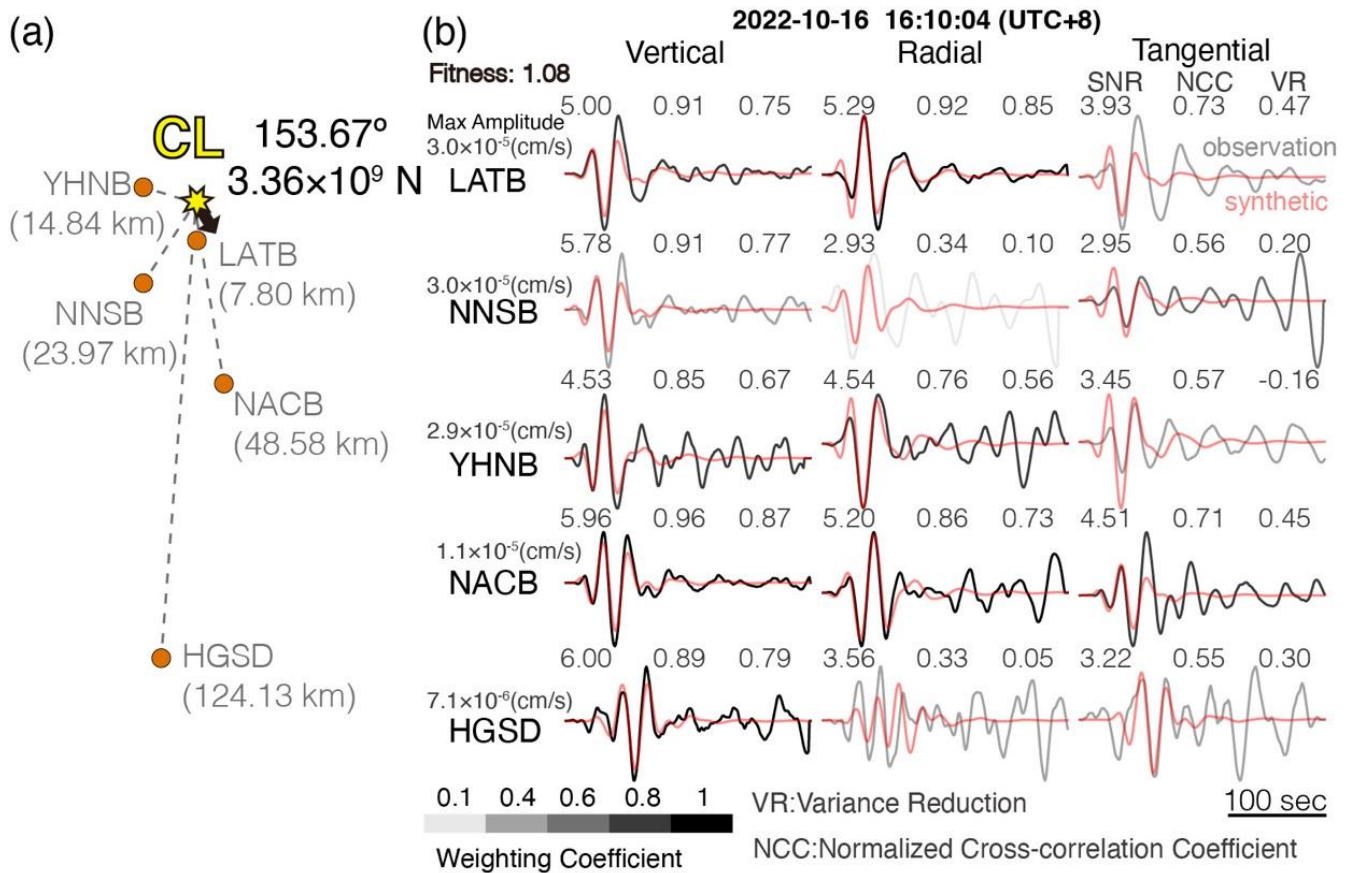
267
 268 Figure 4 Spectrograms of the seismic signal from V03G with the North component. (a) DFT spectrogram
 269 and PSD sum between 16:00-17:00 on 16 October 2022 (UTC+8). (b) Event 1 of DST with linear
 270 frequency axis and DFT with linear frequency and semi-log frequency axes. (c) DST spectrogram with

271 semi-log frequency axes for Event 1. The black dashed line is the lower boundary of the high PS values,
272 showing the V-shaped spectrogram feature. The purple points are the lowest points of the four V-shapes
273 that separate the first half (I), the acceleration phase, from the second half (II), the deceleration phase.
274 The blue numbers indicate a sequence of the V-shapes. (d) Spectrogram of DST for Event 2. The black
275 rectangles mark the spectrogram feature. (e) DST spectrogram for Event 3. The horizontal orange bars
276 below the x-axis in (c)(d)(e) are the signal windows for particle motion analysis in Fig. 10.

277 Except for Events 1 to 3, Fig. 4a exhibited two spikes. We examined the corresponding
278 spectrograms and found that the signals were faint and heavily obscured by ambient noise (Fig. S4).
279 Consequently, the evidence derived from these indirect observations does not substantiate their origin
280 from landslide activity.

281 **4.2 Single-force inversion for the CL**

282 We employed an SF approach for Event 1 of the CL, utilizing a network of five seismic stations
283 (Fig. 5a). Source-station distances spanned from 7.80 km to 124.13 km, and back azimuths ranged from
284 170° to 296°. After testing several starting times of the seismic signals for the SF, we found that signals
285 starting at 16:10:04 yielded the best results. The normalized cross-correlation coefficient and the variance
286 reduction of these signals averaged 0.72 and 0.74, respectively (Fig. 5b). The overall performance
287 exhibited a fitness value 1.08. Subsequently, the SNR values ranged from 2.93 to 6.00, and the NACB
288 consistently exhibited a relatively high SNR across the three components. The inversion process yielded
289 a force direction of 153.67° and a force magnitude of 3.36×10^9 (Newton). The magnitude of the force was
290 converted into landslide mass using an empirical formula, and the landslide volume was estimated to be
291 approximately 523,540 m³.



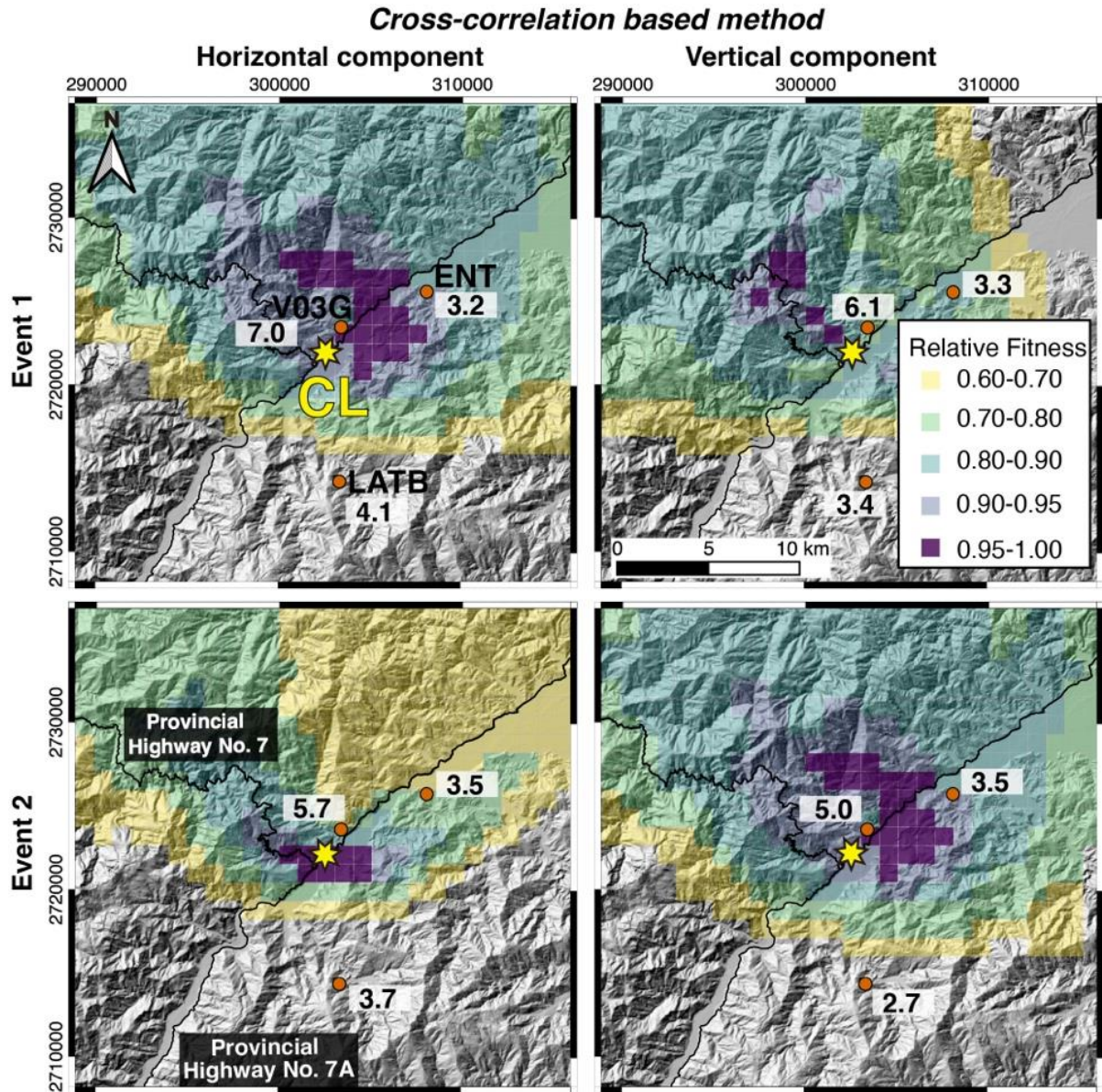
292

293 Figure 5 (a) Position of seismic stations relative to the CL. The black arrow indicates the inverted force
 294 direction of 153.67° with a force magnitude of 3.36×10^9 (Newton). (b) Synthetic and observation
 295 waveforms of the CL with SNR, normalized cross-correlation coefficient, and variance reduction. The
 296 grey gradient presents the different weightings to retrieve the fitness corresponding to the SNR of the
 297 signals (Table S2).

298 4.3 Source location

299 The V03G station recorded Events 1 to 3. Assuming these signals originated from the same slope
 300 of landslides, the characteristics of the spectrogram could provide valuable insights into the short-term
 301 behavior of the CL. Therefore, to determine the locations of Events 1 to 3, we utilized the GeoLoc method.
 302 The results of Events 1 and 2 of the CC, considering both the horizontal and vertical components,
 303 indicated that the grids with high fitness values (> 0.95) were close to the V03G station (Purple grid cells
 304 in Fig. 6). In addition, the ASL tended to be near the station with the highest amplitude (Fig. S5).

305 Therefore, Events 1 and 2 probably originated from the same landslide location. For Event 3, the signals
 306 were too weak to be detected by the ENT and LATB stations. Only V03G recorded its signals, which
 307 supports the location of Event 3 near the V03G station.



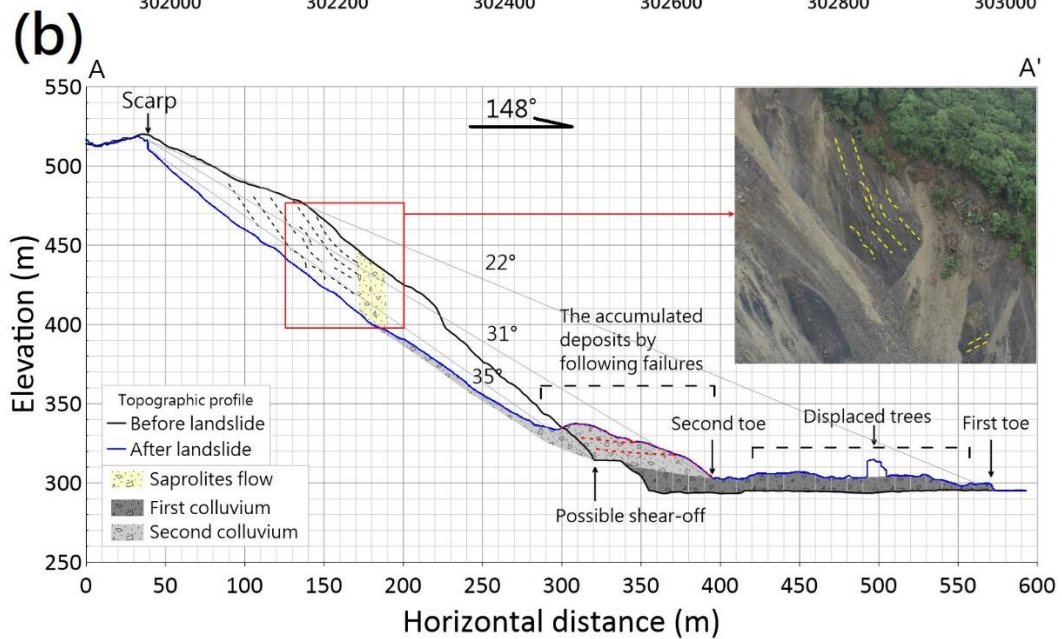
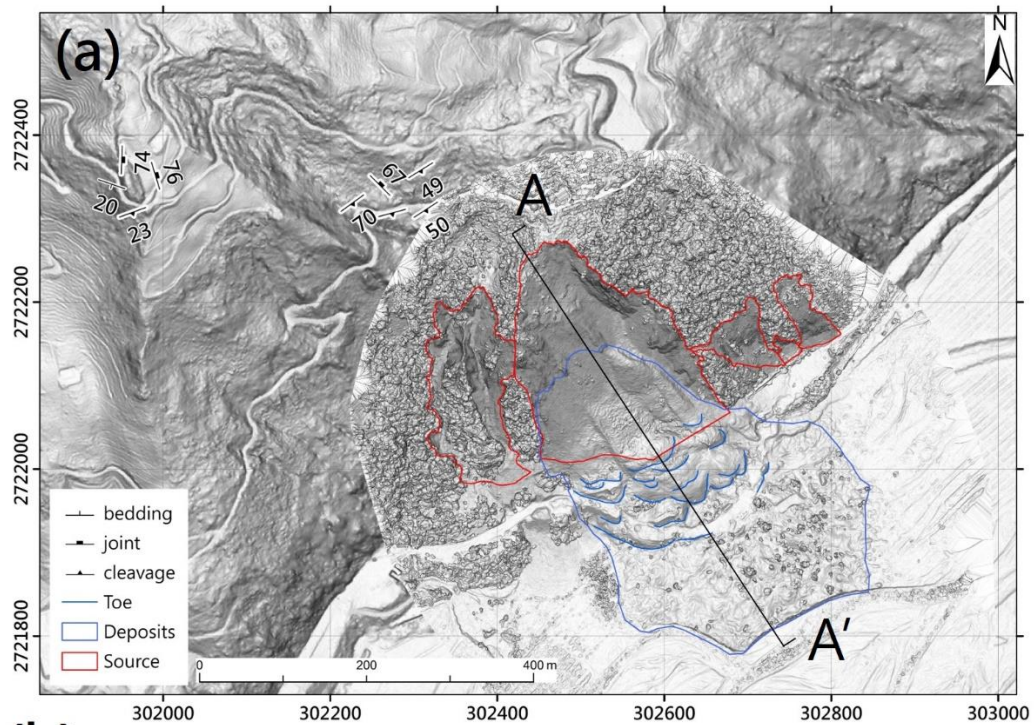
308
 309 Figure 6 Location determination by cross-correlation-based method of horizontal and vertical component
 310 data for Event 1 and Event 2. The values following the stations with transparent white backgrounds are
 311 SNR.

312 **4.4 Landslide survey**

313 According to the topographic profile (A-A' in Fig. 7a), the sliding direction was approximately
314 148°, similar to the result obtained from the SF (153.67°). The observed elevation difference and travel
315 distance of the CL were 220 m and 530 m, respectively. The apparent friction angle ranged from 22° to
316 31°, transitioning from the main scarp to the first significant and subsequent failures (Fig. 7b). This
317 variation could be attributed to the depositional environments and landslide volumes.

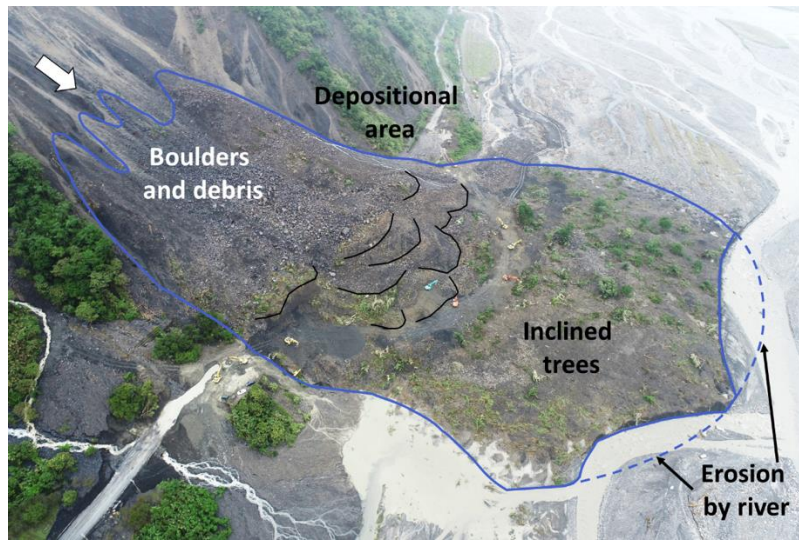
318 Furthermore, we compared the topographical profiles before (1m high-resolution LiDAR data in
319 2014) and after (**drone-derived DSM**) the CL. The data revealed that the maximum erosion depth
320 approached approximately 45 m near the left flank of the CL, where the bedrock was exposed. For the
321 location, photographic evidence shows that the dips of slate cleavage exhibited a gradual transition from
322 steep (at the top) to gentle (at the bottom) (Fig. 7b). This characteristic indicated gravitational slope
323 deformation (Chigira, 1992; Agliardi et al., 2001), suggesting a weakening of the structural integrity and
324 strength of the rock mass constituting the slope. The CL originated from a source area measuring 44,562
325 m² and was deposited over an area of 94,396 m², resulting in a maximum colluvium thickness of 30 m
326 (Fig. 7b). The calculated source volume by difference of elevation was approximately 664,926 m³.
327 Consequently, the landslide mass was converted into a deposited volume of 690,445 m³.

328 The slope map of DSM exhibited deposits with imbrication-like features at the landslide toe,
329 which was covered on the wider and flatter colluvium with the first toe. This pattern was contributed to
330 by the widespread colluvium area where numerous trees rest on the colluvium, composed of slate boulders,
331 debris, saprolites, and soils (Figs. 7b and 8). The inclined trees on the colluvium imply the colluvium is
332 displaced with slight disturbance due to the low-friction basal detachment. The imbricated deposits near
333 the original roadside slope represented a depositional sequence resulting from later failures. The result of
334 the geological investigation shows that the dip direction of the slate cleavage corresponded to the slope
335 aspect and sliding direction, with a high dip angle influencing CL failure (Fig. 7b). Additionally, before
336 the occurrence of the CL, an inspection conducted in May 2022 revealed slight damage and displacement
337 of the downslope concrete wall near the slope (Figs. 9a-9e). These damage signs served as early indicators
338 of creeping slope.



339

340 Figure 7 (a) Topographic feature interpretation on drone-based slope map after landslide (19 October
 341 2022). (b) Topographic profile of AA'. The embedded drone photos show the slate outcrop on the left
 342 flank of the landslide. The dashed curves indicate that the dip angle and traces of cleavages changed and
 343 deformed.



344

345 Figure 8 The closed aerial photo of CL deposits. The imbrication-like features are lineated by black lines.
 346 The first toe was eroded by river.



347

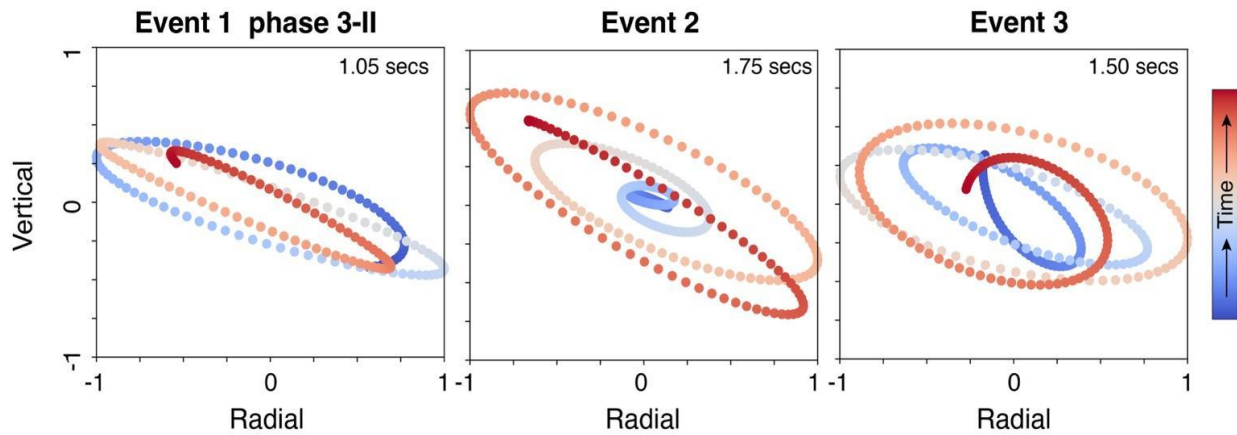
348 Figure 9 (a) Google Earth image before the CL. (b)-(e) Photos from inspection on 27 May 2022. (f) Drone-
 349 based 3-dimensional model after the CL. (g)-(j) Photos of crown cracks of the CL.

350 **5. Discussion**

351 **5.1 Source location of landslide signals**

352 Assuming that Event 1 to Event 3 originated from the slope of the CL, we performed a particle
353 motion analysis within 1 Hz to 3 Hz of V03G (back azimuth: 208°) to clarify their source locations. Given
354 the surface behavior of the landslides, our analysis focused on the vertical and radial components
355 associated with the propagation of Rayleigh waves. Regarding Event 1, we observed intricate patterns of
356 particle motion, particularly during phase 1 of the sliding (Fig. S6). While the initial sliding phase of
357 Event 1 indicated significant movement, the event was governed by a single force mechanism. However,
358 not all materials involved in the landslide exhibited pure shear sliding. Some materials were bouncing,
359 rolling, or interacting with the ground, slopes, and adjacent particles. These physical processes could
360 generate high-frequency signals, resulting in complex and inexplicable particle motion patterns from
361 phase 1 to phase 2 of Event 1. In contrast, the particle motion displayed a more consistent direction during
362 the small-scale mass movement observed in phases 3 and 4, which manifested as clear ellipses. Notably,
363 the ellipse corresponding to phase 3-II of Event 1 was particularly pronounced and linked to Events 2 and
364 3 (Fig. 10). These elliptical patterns indicated retrograde motion along the travel direction.

365 Further, we investigated the relationship between different back azimuths and elliptical shapes.
366 When the back azimuth was set at 228°, the elliptical shapes showed a noticeable change (Fig. S7a).
367 However, similar elliptical shapes were consistently observed for back azimuth values ranging from 188°
368 to 148° (Figs. S7b-c). This suggests that elliptical shapes do not exhibit significant sensitivity within 208°
369 to 148°, where sources could potentially originate from a wide back azimuth range. Nevertheless, no
370 documented landslides are reported during the range of back azimuth between 208° to 148° (Fig. S8);
371 most substantial landslides are oriented with back azimuth angles greater than 228° (Fig. 2). Subsequently,
372 the CC and ASL results indicated that Event 2 is close to V03G. Therefore, we posit that at least Event 1
373 and Event 2 likely originated from the same source direction. Event 3, the minor event, challenges
374 determining its precise location by seismic analysis.



375

376 Figure 10 Particle motion comparison between radial and vertical components for phase 3-II of Event 1,
 377 Event 2, and Event 3. The duration of particle motion signals is indicated in the upper right corner of each
 378 subfigure, with precise timing details highlighted by orange bars in Fig.4.

379 5.2 Comprehensive information from seismic analysis

380 When Event 1 and Event 2 occurred on the same slope, we estimated the approximate volume of
 381 the CL using empirical regressions. Event 1 indicated a volume of $523,540 \text{ m}^3$ based on empirical
 382 regression (mass = $0.405 \times$ force magnitude; Chao et al., 2016) for large-scale landslides with a sliding
 383 direction of 153.67° (Table 1). By retrieving the amplitude at the source (A_0 ; unit: cm s^{-1}) through 1-8 Hz
 384 of horizontal signals, we estimated the volume of Event 2 is $16,791 \text{ m}^3$ (Volume= $77,290 A_0^{0.44}$; Chang
 385 et al., 2021). The total volume obtained from a seismic analysis output of $540,331 \text{ m}^3$ is around 19%
 386 lower than the volume estimated by the difference between LiDAR and DSM.

387 Seismic signal analysis provides valuable insight into potential landslide processes. The SF
 388 method detailed the timing and movement direction. The DST spectrogram analysis revealed distinct
 389 timeframes and physical patterns of the three events associated with slope failure. Event 1 likely involved
 390 four sliding failures within 30 seconds with gradually decreasing masses. However, the landslide video
 391 captured the process, lasting approximately 34 seconds for probable phases 2 and 3 in Event 1. This
 392 discrepancy in timing may be attributed to the weak kinetic energy during the early and termination stages
 393 of the CL. The ground vibration signal at those stages might not transmit to V03G, potentially influencing

394 the recorded duration. Subsequently, Event 2 featured 30s of continuous rockfall, followed by a toppling
395 event with a larger mass.

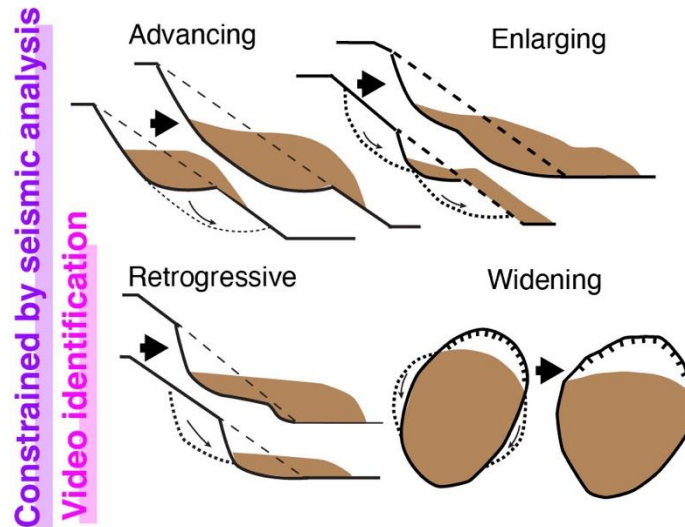
396 **Table 1** Pre-survey information of the CL by seismic analysis

Landslide characteristics	Information	
	Event 1	Event 2
Occurrence time	4:10 PM on 16 October 2022.	4:30 PM on 16 October 2022
Estimated volume	523,540 m ³	16,791 m ³
Sliding direction	153.67°	-
Failure process	Four continuous sliding with the gradual reduction in sliding volume	Rockfall and toppling

397

398 **5.3 Landslide evolution model**

399 Landslides are categorized into seven movement types (Varnes, 1978). According to the
400 spectrogram features of Event 1 in the CL, this seismic analysis preferred sliding movement. The stepwise
401 failure process of a landslide can be determined based on the distribution of landslide activity, such as
402 advancing, retrogressive, enlarging, or widening activities (Fig. 11) (WP/WLI, 1993). Advancing and
403 retrogressive activity involves the expansion of the rupture surface along and in the opposite direction of
404 movement. Enlargement entails the rupture surface expanding in multiple directions, whereas widening
405 indicates that the rupture surface extends into one or both flanks of the landslide.



406

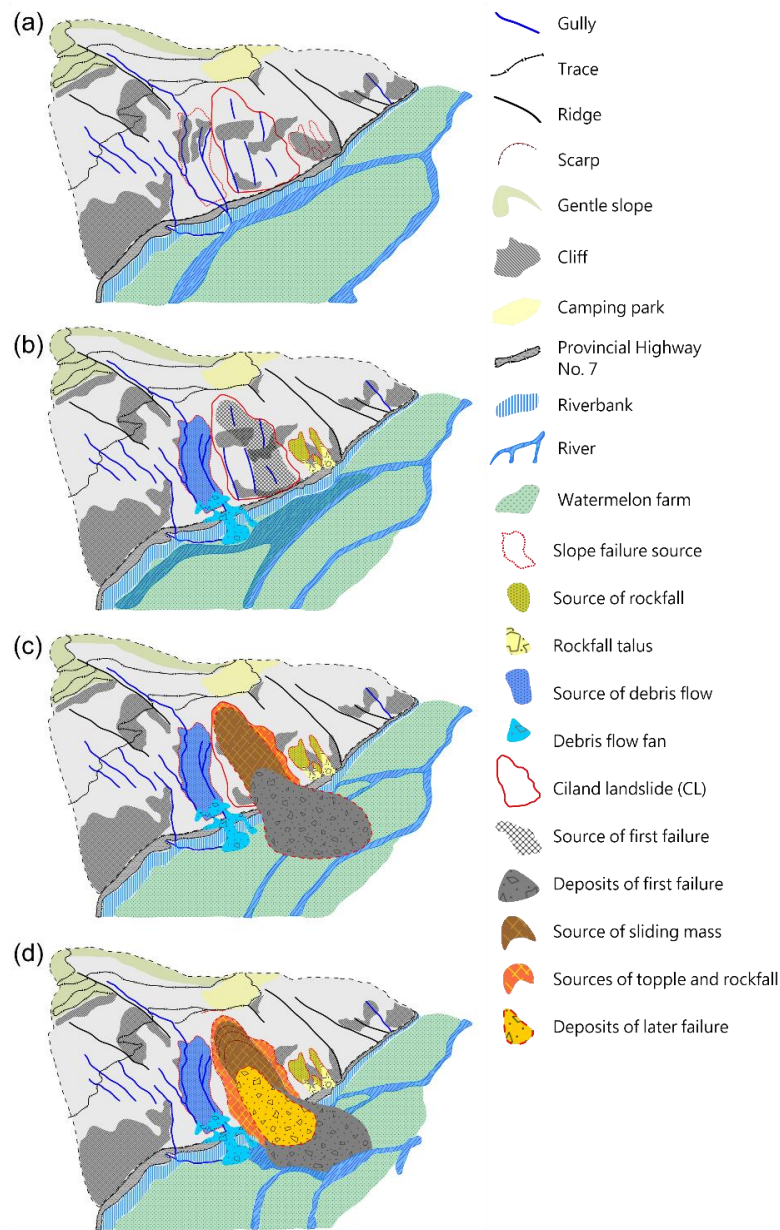
407 Figure 11 Schematic diagram of potential landslide activities for the CL. Dot lines represent the
 408 detachments in the next stage. Dash lines indicate the original ground level. The brown color indicates
 409 the extent of displaced material. The figure has been modified from Cooper (2007).

410 For the CL, the left flank was exposed at the beginning of the video (Fig. S2), which implies
 411 previous failures had occurred earlier than the beginning of the video. It is reasonable that people were
 412 attracted by previous failures and prepared to take videos for subsequent failures. Besides, the debris flow
 413 had deposited a debris fan on the road (Fig. 2h), and excavators were operated to clear the buried road
 414 section. The moving mass from the upslope was sliding downward and pushing the previous colluvium.
 415 Moreover, some trees displaced to downslope on the top of moving mass, which implies a similar
 416 phenomenon during early failure with similar landslide source conditions (Fig. 7). Consequently, the
 417 video recorded the process of sliding that could correspond to the distribution and geometry of deposits
 418 (Figs. 7 and 8) and validate the sliding of Event 1 by seismic analysis (Fig. 4d).

419 Combining the pre-survey understanding with the survey results, the initial model for landslide
 420 evolution was established (Fig. 12a). According to the announces of the Directorate General of Highways
 421 in Taiwan (Table S1) and the CL occurrence time extracted by seismic analysis, the debris flow and
 422 rockfall were induced by heavy rainfall before the CL (Fig. 12b). The initial failure mechanism of the CL
 423 could be assumed to initiate at a shear-off from the original toe (roadside slope) caused by the high pore-
 424 water pressure after heavy rainfall infiltration. The first failure should deposit on sandy and gravelly

425 alluvial deposits with high water levels (Fig. 12b). The rapid loading of sliding mass onto the wet alluvial
426 deposits may have induced liquefaction and reduced the basal friction of sliding mass (Sassa, 1992). The
427 first failure had the most significant volume, leading to higher mobility (Figs. 7, 8, and 12c) (Corominus,
428 1996; Legros, 2002; Hungr and Evans, 2004). It possibly corresponds to Phase 1 of Event 1 in Table S1.
429 However, for subsequent failures (Phases 2-4 of Event 1), failure masses were deposited on the angular
430 debris and boulders of the previous colluvium, characterized by a rough ground surface, resulting in lower
431 mobility (Fig. 12d). This process of retrogression may be captured in the video (Fig. S2). Therefore, the
432 most plausible landslide activities could be retrogression in Event 1. Then, the widening activity
433 developed by toppling and rockfalls with subsequent Event 2, Event 3, and other failures from the steep
434 scarp and flanks (Fig. 11) (refers to YouTube video: <https://www.youtube.com/watch?v=PMlb7OiCqMQ>;
435 last access on 30 October 2024).

436 The continuous presence of the four phases in Event 1 (Fig. 4b) and the field survey imply a
437 fractured bedrock/steep sliding surface near the CL. Following the landslide, steep scarps and flanks
438 emerged, exhibiting discontinuities such as cleavage, joints, and numerous tension cracks at the crown
439 (Figs. 9f-9j). This observation suggests the potential for further enlargement of the landslide. An unstable
440 slope directly threatened the safety of residents living close to the crown of the CL. Therefore, it is
441 imperative to implement comprehensive monitoring measures on the slopes described by Kang et al.
442 (2021). These measures are essential for gaining a deeper understanding of ongoing landslide activity and
443 ensuring the safety of the affected population.



444

445 Figure 12 The geological model and topographic evolution of the CL. (a) The initial model is based on
 446 LiDAR topographic features. (b) According to Fig. 2 and Table S1, slope failures (debris flow and
 447 rockfalls) occurred around the CL. (c) The failure process of Phase 1 of Event 1 of the CL is based on
 448 Figs. 4 and 7 and Table 1. (d) The final stage of the CL, after Phases 2-4 of Event 1, Events 2 and 3 of
 449 the CL.

450 **5.4 Future Perspective**

451 The research demonstrates that seismic signal analysis provides geologists with timely
452 information prior to field surveys, which is important in Taiwan. As a narrow island, Taiwan relies heavily
453 on its provincial highways, especially the cross-island routes, for transportation. When landslides block
454 these roads, the Highway Bureau of Taiwan must quickly remove the debris to reopen the routes. As a
455 result, the post-landslide topography often changes during these engineering activities. In this study, for
456 example, the field survey was conducted three days after the CL, by which time excavators had already
457 altered some of the post-landslide deposits (Figure 8). Although seismic analysis has limitations in
458 providing precise sliding direction, volume estimation, and understanding the physical process (Gualtieri
459 and Ekström, 2018; Li et al., 2018; Chang et al., 2024), it offers sufficient preliminary information to
460 assess the landslide's characteristics before more detailed fieldwork.

461 Looking ahead to medium and small landslide monitoring, high-frequency seismic signal analysis
462 (>1 Hz) yields similar results, except for sliding direction, which remains challenging to determine. This
463 limitation arises from the development of high-frequency Green's functions used to examine the force
464 mechanism. Consequently, both low- and high-frequency seismic analysis algorithms can be flexibly
465 applied depending on the monitoring objectives. Chang et al. (2024) have addressed relevant applications
466 of this approach.

467 Additionally, during a seasonal inspection on May 27, 2022, prior to the CL, the downslope
468 concrete wall was found to be slightly damaged and displaced (Figs. 9a-9e). This highlights the
469 importance of regular roadside slope inspections. To face a similar situation in the future, techniques such
470 as seismic ambient noise analysis (Colombero et al., 2021; Le Breton et al., 2021) and remote monitoring
471 systems (Squarzoni et al., 2020) can be considered for long-term surveillance. The CL also caused
472 numerous crown cracks (Figs. 9f-9j), posing additional risks of further failures that threaten the safety of
473 residents living upslope. Comprehensive monitoring is, therefore, essential to better understand ongoing
474 landslide activity and mitigate future risks (Kang et al., 2021).

475 **6. Conclusions**

476 Research on the Cilan Landslide (CL) has shown how to deliver seismic analysis results as pre-
477 survey knowledge to geologists for field surveys. We investigated a series of events involving the efficient
478 generation of one-hour spectrograms through a discrete Fourier transform. Three events, Event 1, Event
479 2, and Event 3, were identified, with four continuous phases of sliding, rockfall, and the subsequent
480 toppling and rockfalls, as revealed by the spectrograms obtained via a Stockwell transform with a semi-
481 log frequency axis. The initial sliding of the CL generated low-frequency seismic signals (ranging from
482 0.02 Hz to 0.05 Hz), and we successfully determined an inverted single force direction of 153.67° , close
483 to the actual direction of landslide movement, which was 148° . This geohazard location (GeoLoc)
484 pinpointed Event 1 and Event 2 close to seismic station V03G, whereas a polarization analysis provided
485 further support for the notion that these event sources may have originated from the same direction,
486 indicating a high probability of sharing the same slope of origin. Additionally, by employing the force
487 magnitude and amplitude at the source (A_0) in the empirical regressions for Event 1 and Event 2 of the
488 CL, we estimated the landslide volume to be $540,331 \text{ m}^3$, 19% lower than the volume calculated using a
489 digital elevation model.

490 This information has significantly contributed to geologists' understanding of the physical
491 processes underlying the CL for predicting advancing, retrogressive, enlarging, or widening mechanisms.
492 After combining the field survey, the seismic analysis results have led geologists to propose a detailed
493 mechanism for the CL. This mechanism involves shear-off from the roadside slope and subsequent mass
494 sliding triggered by high pore-water pressure from rainfall infiltration. The observed physical behaviors
495 of subsequent failures and topographic features with imbrication-like deposits suggest that the most
496 plausible landslide activity may undergo retrogression and widening over time.

497 The research supported the idea that seismic analysis enables the determination of a landslide's
498 inverted-force direction, estimated landslide volume, and physical processes. Notably, seismic analysis
499 from an adjacent station provides additional temporal insight into landslides' dynamics, whereas
500 geological surveys can only investigate the topography post-landslide to constrain the failure mechanisms.
501 Therefore, seismic analysis provides crucial information for geologists before conducting field surveys.

502 **Data availability**

503 Waveform data for this study were provided by the Broadband Array in Taiwan for Seismology (BATS;
504 <https://doi.org/10.7914/SN/TW>, Academia Sinica, Institute of Earth Sciences, 1996.) and the Central
505 Weather Administration, Taiwan (CWA; <https://doi.org/10.7914/SN/T5>). The raw seismic data of V03G
506 is available through Figshare (<https://doi.org/10.6084/m9.figshare.24464281.v1>). The digital terrain
507 model (DTM) of the 20-meter resolution used in Fig. 2 is available from the Government Open Data
508 Platform, Taiwan (<https://data.gov.tw/dataset/35430>; Ministry of the Interior, 2024). The road shape files
509 are available from the National Land Surveying and Mapping Center, Taiwan
510 (http://maps.nlsc.gov.tw/S_Maps/wms). The last accessed of all URLs was on 30 October 2024.

511 **Competing interests**

512 The contact author has declared that none of the authors has competing interests.

513 **Author contribution**

514 JM and CM conceived of the presented idea and wrote the manuscript. WA supervised the project,
515 provided critical feedback, and helped shape the research, analysis, and manuscript. JM, CM, WA, and
516 MW carried out the field investigations. CS, MW, TC, and CY discussed the results and contributed to
517 the final manuscript.

518 **Acknowledgments**

519 The authors acknowledged the National Science and Technology Council of Taiwan (NSTC) for the
520 funding support. The authors acknowledge the Forestry and Nature Conservation Agency, Taiwan for
521 providing LiDAR data and the Geological Survey and Mining Management Agency, Taiwan for LiDAR
522 data establishment. **We also acknowledged the editor, Dr. Daniele Giordan, and two reviewers's feedback,**
523 **which greatly improved the paper's quality.**

524 **Financial support**

525 This study is financially supported by the National Science and Technology Council of Taiwan (NSTC)
526 for Che-Ming Yang under grants NSTC 110-2116-M-239-001-MY2, NSTC- 112-2116-M-239-001,
527 NUU project No. SM113004 and We-An Chao under grants NSTC 111-2625-M-A49-004-MY3.

528 **References**

- 529 Agliardi, F., Crosta, G., and Zanchi, A.: Structural constraints on deep-seated slope deformation
530 kinematics, *Eng. Geol.*, 59(1-2), 83-102, [https://doi.org/10.1016/S0013-7952\(00\)00066-1](https://doi.org/10.1016/S0013-7952(00)00066-1), 2001.
- 531 Aki, K. and Ferrazzini, V.: Seismic monitoring and modeling of an active volcano for prediction, *J.*
532 *Geophys. Res.*, 105, 16617–16640, <https://doi.org/10.1029/2000JB900033>, 2000.
- 533 Allstadt, K.: Extracting source characteristics and dynamics of the August 2010 Mount Meager landslide
534 from broadband seismograms, *J. Geophys. Res.*, 118, 1472–1490, <https://doi.org/10.1002/jgrf.20110>,
535 2013.
- 536 Brodsky, E. E., Gordeev, E., and Kanamori, H.: Landslide basal friction as measured by seismic waves,
537 *Geophys. Res. Lett.*, 30, 2236, <https://doi.org/10.1029/2003GL018485>, 2003.
- 538 Chang, J.M., Chao, W.A., Chen, H., Kuo, Y.T., and Yang, C.M.: Locating rock slope failures along
539 highways and understanding their physical processes using seismic signals, *Earth Surf. Dynam.*, 9,
540 505–517, <https://doi.org/10.5194/esurf-9-505-2021>, 2021.
- 541 Chang, J.M., Chao, W.A., Kuo, Y.T., Yang, C.M., Chen, H., and Wang, Yu.: Field experiments: How
542 well can seismic monitoring assess rock mass falling? *Eng. Geol.*, 323, 107211,
543 <https://doi.org/10.1016/j.enggeo.2023.107211>, 2023.
- 544 Chang, J. M., Kuo, Y. T., Chao, W. A., Lin, C. M., Lan, H. W., Yang, C. M., & Chen, H.: Landslide
545 Warning Area Delineation through Seismic Signals and Landslide Characteristics: Insights from the
546 Silabaku Landslide in Southern Taiwan. *Seismol. Res. Lett.*, 95(5), 2986-2996,
547 <https://doi.org/10.1785/0220230396>, 2024.
- 548 Chao, W.A., Zhao, L., Chen, S.C., Wu, Y.M., Chen, C.H., and Huang, H.H.: Seismology-based early
549 identification of dam-formation landslide events, *Sci. Rep.*, 6, 19259,
550 <https://doi.org/10.1038/srep19259>, 2016.

- 551 Chao, W.A., Wu, Y.M., Zhao, L., Chen, H., Chen, Y.G., Chang, J.M., and Lin, C.M.: A first near real-
552 time seismology-based landquake monitoring system, *Sci. Rep.*, 7, 43510,
553 <https://doi.org/10.1038/srep43510>, 2017.
- 554 Chao, W.A., Wu, T.R., Ma, K.F., Kuo, Y.T., Wu, Y.M., Zhao, L., Chung, M.J., Wu, H., and Tsai, Y.L.:
555 The large Greenland landslide of 2017: Was a tsunami warning possible? *Seismol. Res. Lett.* 89(4),
556 1335-1344. <https://doi.org/10.1785/0220170160>, 2018.
- 557 Chen, C.-H., Chao, W.A., Wu, Y.M., Zhao, L., Chen, Y.G., Ho, W.Y., Lin, T.L., Kuo, K.H., and Chang,
558 J.M.: A seismological study of landquakes using a real-time broad-band seismic network, *Geophys.*
559 *J. Int.*, 194, 885–898, <https://doi.org/10.1093/gji/ggt121>, 2013.
- 560 Chen, L.C.: Action Plan for Prevention and Control of Large-Scale Landslide Disasters (In Chinese),
561 National Science and Technology Center for Disaster Reduction, Taiwan, <https://reurl.cc/M8anXL>,
562 2015.
- 563 Chigira, M.: Long-term gravitational deformation of rocks by mass rock creep. *Eng. Geol.*, 32, 157-184,
564 [https://doi.org/10.1016/0013-7952\(92\)90043-X](https://doi.org/10.1016/0013-7952(92)90043-X), 1992.
- 565 Colombero, C., Jongmans, D., Fiolleau, S., Valentin, J., Baillet, L., & Bièvre, G.: Seismic noise
566 parameters as indicators of reversible modifications in slope stability: a review. *Surveys in*
567 *Geophysics*, 42, 339-375, <https://doi.org/10.1007/s10712-021-09632-w>, 2021.
- 568 Cooper, R.G. 2007. Mass Movements in Great Britain, Geological Conservation Review Series, No. 33,
569 Joint Nature Conservation Committee, Peterborough, 348 pp.
- 570 Dammeier, F., Moore, J.R., Haslinger, F. and S. Loew: Characterization of alpine rockslides using
571 statistical analysis of seismic signals, *J. Geophys. Res.*, 116, F04024,
572 <https://doi:10.1029/2011JF002037>, 2011.
- 573 Dietze, M., Turowski, J. M., Cook, K. L., and Hovius, N.: Spatiotemporal patterns, triggers and anatomies
574 of seismically detected rockfalls, *Earth Surf. Dynam.*, 5, 757–779, [https://doi.org/10.5194/esurf-5-](https://doi.org/10.5194/esurf-5-757-2017)
575 [757-2017](https://doi.org/10.5194/esurf-5-757-2017), 2017.

- 576 Ekström, G. and Stark, C. P.: Simple scaling of catastrophic landslide dynamics, *Science*, 339, 1416–
577 1419, <https://doi.org/10.1126/science.1232887>, 2013.
- 578 Fei, L.Y., Chen, M.M.: Geological investigation and database construction for upstream of flood-prone
579 area – maps and explanatory text (In Chinese). Central Geological Survey, MOEA, Taiwan, 192,
580 2013.
- 581 Feng, Z.: The seismic signatures of the 2009 Shiaolin landslide in Taiwan, *Nat. Hazards Earth Syst. Sci.*,
582 11, 1559–1569, <https://doi.org/10.5194/nhess-11-1559-2011>, 2011.
- 583 Fuchs, F., Lenhardt, W., Bokelmann, G., and the AlpArray Working Group: Seismic detection of
584 rockslides at regional scale: examples from the Eastern Alps and feasibility of kurtosis-based event
585 location, *Earth Surf. Dynam.*, 6, 955–970, <https://doi.org/10.5194/esurf-6-955-2018>, 2018.
- 586 Guinau, M., Tapia, M., Pérez-Guillén, C., Suriñach, E., Roig, P., Khazaradze, G., Torné, M., Royán, M.
587 J., and Echeverria, A.: Remote sensing and seismic data integration for the characterization of a rock
588 slide and an artificially triggered rock fall, *Eng. Geol.*, 257, 105113,
589 <https://doi.org/10.1016/j.enggeo.2019.04.010>, 2019.
- 590 **Gualtieri, L., and Ekström, G.: Broad-band seismic analysis and modeling of the 2015 Taan Fjord, Alaska**
591 **landslide using Instaseis. *Geophysical Journal International*, 213(3), 1912-1923,**
592 **<https://doi.org/10.1093/gji/ggy086>, 2018.**
- 593 Hibert, C., Ekström, G., and Stark, C. P.: Dynamics of the Bingham Canyon Mine landslides from seismic
594 signal analysis, *Geophys. Res. Lett.*, 41, 4413-4804, <https://doi.org/10.1002/2014GL060592>, 2014.
- 595 Hibert, C., Stark, C. P., and Ekström, G.: Dynamics of the Oso-Steelhead landslide from broadband
596 seismic analysis, *Nat. Hazards Earth Syst. Sci.*, 15, 1265–1273, [https://doi.org/10.5194/nhess-15-](https://doi.org/10.5194/nhess-15-1265-2015)
597 [1265-2015](https://doi.org/10.5194/nhess-15-1265-2015), 2015.
- 598 Hungr, O., and Evans, S.G.: Entrainment of debris in rock avalanches: An analysis of a long run-out
599 mechanism. *GSA Bulletin*, 116 (9-10), 1240–1252. <https://doi.org/10.1130/B25362.1>, 2004.

- 600 Hungr, O., Leroueil, S., and Picarelli, L.: The Varnes classification of landslide types, an update.
601 Landslides 11, 167–194, <https://doi.org/10.1007/s10346-013-0436-y>, 2014.
- 602 Kanamori, H., and Given, J. W.: Analysis of long-period seismic waves excited by the May 18, 1980,
603 eruption of Mount St. Helens - A terrestrial monopole?, J. Geophys. Res., 87, 5422–5432,
604 doi:10.1029/JB087iB07p05422, 1982.
- 605 Kang, K.H., Chao, W.A., Yang, C.M., Chung, M.C., Kuo, Y.T., Yeh, C.H., Liu, H.C., Lin, C.H., Lin, C.P.,
606 Liao, J.J., Chang, J.M., Ngui, Y.N., and Tai, T.L.: Rigidity Strengthening of Landslide Materials
607 Measured by Seismic Interferometry. Remote Sens. 13(14), 2834.
608 <https://doi.org/10.3390/rs13142834>, 2021.
- 609 Kao, H., Jian, P.R., Ma, K.F., Huang, B.S. and Liu, C.C.: Moment-tensor inversion for offshore
610 earthquakes east of Taiwan and their implications to regional collision. Geophys. Res. Lett., 25,
611 3619-3622. <https://doi.org/10.1029/98GL02803>, 1998.
- 612 Kuo, H.L., Lin, G.W., Chen, C.W., Saito, H., Lin, C.W., Chen, H., and Chao, W.A.: Evaluating critical
613 rainfall conditions for large-scale landslides by detecting event times from seismic records, Nat.
614 Hazards Earth Syst. Sci., 18, 2877–2891, <https://doi.org/10.5194/nhess-18-2877-2018>, 2018.
- 615 Le Breton, M., Bontemps, N., Guillemot, A., Baillet, L., & Larose, É.: Landslide monitoring using seismic
616 ambient noise correlation: challenges and applications. Earth-Science Reviews, 216, 103518,
617 <https://doi.org/10.1016/j.earscirev.2021.103518>, 2021.
- 618 Legros, F.: The Mobility of Long-Runout Landslides. Eng. Geol., 63, 301-331.
619 [http://dx.doi.org/10.1016/S0013-7952\(01\)00090-4](http://dx.doi.org/10.1016/S0013-7952(01)00090-4), 2002.
- 620 Li, W., Zhang, Y., Xu, Y., Zheng, X., Wang, R., Su, J., Yi, G., and Huang, Q.: Complex dynamics of
621 repeating and river-blocking landslides in Jiangda during 2018, Earthq. Sci., 34(1),
622 <https://doi.org/10.29382/eqs-2020-0034>, 3-14, 2021.

- 623 Manconi, A., Mondini, A. C., and the AlpArray working group: Landslides caught on seismic networks
624 and satellite radars, *Nat. Hazards Earth Syst. Sci.*, 22, 1655–1664, [https://doi.org/10.5194/nhess-22-](https://doi.org/10.5194/nhess-22-1655-2022)
625 [1655-2022](https://doi.org/10.5194/nhess-22-1655-2022), 2022.
- 626 Moretti, L., Mangeney, A., Capdeville, Y., Stutzmann, E., Huggel, C., Schneider, D., and Bouchut, F.:
627 Numerical modeling of the mount Steller landslide flow history and of the generated long period
628 seismic waves. *Geophys. Res. Lett.*, 39, L16402, <https://doi.org/10.1029/2012GL052511>, 2012.
- 629 Provost, F., Malet, J.-P., Hibert, C., Helmstetter, A., Radiguet, M., Amitrano, D., Langet, N., Larose, E.,
630 Abancó, C., Hürlimann, M., Lebourg, T., Levy, C., Le Roy, G., Ulrich, P., Vidal, M., and Vial, B.:
631 Towards a standard typology of endogenous landslide seismic sources, *Earth Surf. Dynam.*, 6, 1059-
632 1088, <https://doi.org/10.5194/esurf-6-1059-2018>, 2018.
- 633 Sassa, K.: Landslide volume–apparent friction angle relationship in the case of rapid loading on alluvial
634 deposits. *Landslide News* 6, 16 – 19, 1992.
- 635 Shin, T.C., and Chen, Y.L.: Study of earthquake location of 3-D velocity structure in Taiwan area. (In
636 Chinese). *Meteorological Bulletin* 42, 135-169,
637 <https://photino.cwb.gov.tw/rdcweb/lib/cd/cd07mb/MB/PDF/42/No.2/03.pdf>, 1998.
- 638 Squarzoni, G., Bayer, B., Franceschini, S., and Simoni, A.: Pre-and post-failure dynamics of landslides
639 in the Northern Apennines revealed by space-borne synthetic aperture radar interferometry (InSAR).
640 *Geomorphology*, 369, 107353, <https://doi.org/10.1016/j.geomorph.2020.107353>, 2020.
- 641 Suriñach, E., Vilajosana, I., Khazaradze, G., Biescas, B., Furdada, G., and Vilaplana, J. M.: Seismic
642 detection and characterization of landslides and other mass movements, *Nat. Hazards Earth Syst.*
643 *Sci.*, 5, 791–798, <https://doi.org/10.5194/nhess-5-791-2005>, 2005.
- 644 Varnes, D.: Slope movement types and processes. In *Landslides: Analysis and Control* (eds Schuster, R.
645 L. & Krizek, R. J.), Transportation Research Board, National Academy of Science, Washington,
646 1978.

- 647 Vilajosana, I., Suriñach, E., Abellán, A., Khazaradze, G., Garcia, D., and Llosa, J.: Rockfall induced
648 seismic signals: case study in Montserrat, Catalonia, *Nat. Hazards Earth Syst. Sci.*, 8, 805–812,
649 <https://doi.org/10.5194/nhess-8-805-2008>, 2008.
- 650 Walter, F., Burtin, A., McArdell, B. W., Hovius, N., Weder, B., and Turowski, J. M.: Testing seismic
651 amplitude source location for fast debris-flow detection at Illgraben, Switzerland, *Nat. Hazards Earth
652 Syst. Sci.*, 17, 939–955, <https://doi.org/10.5194/nhess-17-939-2017>, 2017.
- 653 Walsh, B., Jolly, A. D., and Procter, J.: Calibrating the amplitude source location (ASL) method by using
654 active seismic sources: An example from Te Maari volcano, Tongariro National Park, New Zealand,
655 *Geophys. Res. Lett.*, 44, 3591–3599, <https://doi.org/10.1002/2017GL073000>, 2017.
- 656 Weng, M.C., Lin, C.H., Shiu, W.J., Chao, W.A., Chiu, C.C., Lee, C.F., Huang, W.K., and Yang, C.M.:
657 Towards a rapid assessment of highway slope disasters by using multidisciplinary techniques,
658 *Landslides*, 19, 687–701, <https://doi.org/10.1007/s10346-021-01808-0>, 2022.
- 659 WP/ WLI. (International Geotechnical Societies UNESCO Working Party on World Landslide Inventory)
660 1993. A suggested method for describing the activity of a landslide. *Bull. Eng. Geol.*, No. 47, 53-57.
- 661 Wu, Y.M., Chang, C.H., Zhao, L., Shyu, J.B.H., Chen, Y.G., Sieh, K., and Avouac, J.P.: Seismic
662 tomography of Taiwan: improved constraints from a dense network of strong-motion stations, *J.
663 Geophys. Res.: Solid Earth*, 112, B08312, <https://doi:10.1029/2007JB004983>, 2007.
- 664 Yamada, M., Kumagai, H., Matsushi, Y., and Matsuzawa, T.: Dynamic landslide processes revealed by
665 broadband seismic records, *Geophys. Res. Lett.*, 40, 2998–3002, doi:10.1002/grl.50437, 2013.
- 666 Yang, C.M., Chang, J.M., Hung, C.Y., Lu, C.H., Chao, W.A. and Kang, K.H.: Life span of a landslide
667 dam on mountain valley caught on seismic signals and its possible early warnings, *Landslides*, 19,
668 637–646, <https://doi.org/10.1007/s10346-021-01818-y>, 2022.